Geophysical Journal International

Geophys. J. Int. (2010) **180,** 251–267 doi: 10.1111/j.1365-246X.2009.04402.x

Estimating Rayleigh wave particle motion from three-component array analysis of ambient vibrations

Valerio Poggi and Donat Fäh

Swiss Seismological Service, ETH Zürich, Switzerland. E-mail: poggi@sed.ethz.ch

Accepted 2009 September 28. Received 2009 September 25; in original form 2008 September 24

SUMMARY

Several methods have been proposed in the past years to extract the Rayleigh wave ellipticity from horizontal-to-vertical spectral ratios of single station ambient noise recordings. The disadvantage of this set of techniques is the difficulty in clearly identifying and separating the contribution of higher modes. In most cases, only the fundamental mode of ellipticity can be identified. Moreover, it is generally difficult to correct for the energy of *SH* and Love waves present in the horizontal components of the ambient vibration wavefield.

We introduce a new methodology to retrieve Rayleigh wave ellipticity using high-resolution frequency–wavenumber array analysis. The technique is applied to the three components of motion and is based on the assumption that an amplitude maximum in the f–k cross-spectrum must represent the true power amplitude of the corresponding signal. In the case of Rayleigh waves, therefore, the ratio between maxima obtained from the horizontal (radial-polarized) and vertical components of motion will also represent the frequency-dependent ellipticity function. Consequently, if we can identify the Rayleigh dispersion curves of several modes on the f–k plane, then the corresponding modal ellipticity patterns can also be separated and extracted.

To test the approach, synthetic and real data sets were processed. In all tested cases, a reliable estimation of segments of the fundamental mode ellipticity was obtained. The identification of higher modes is possible in most cases. The quality of results depends on the selected array geometry and the signal-to-noise ratio, with a major improvement achieved by increasing the number of receivers employed during the survey. An experiment conducted in the town of Visp (Switzerland) allowed the retrieval of portions of ellipticity curves up to the second Rayleigh higher mode, using two concentric circular array configurations of 14 and 11 receivers each.

Key words: Fourier analysis; Earthquake ground motions; Surface waves and free oscillations; Site effects; Computational seismology; Wave propagation.

1 INTRODUCTION

Ambient noise analysis is an easily implemented and economical set of techniques based on passive acquisition and processing of natural and anthropogenic microtremors. These techniques are commonly employed in microzonation and earthquake engineering studies to quickly obtain reliable information about *S*-wave velocity profiles (e.g. Tokimatsu 1997) and soil fundamental frequencies of resonance (e.g. Nakamura 1989). Despite their poor resolution in discriminating between small variations in geophysical properties, these methodologies are in some cases preferable to other types of high-resolution seismic surveys. The low frequency energy content of the ambient noise wavefield allows investigation of deep layers (Yamanaka *et al.* 1994). This characteristic is particularly suited to site effect analysis and when it is useful to evaluate, even if coarsely, the soil deposit properties up to or sometimes below the bedrock limit. Moreover, employing passive source techniques is preferable in urban areas or in any situation where invasive procedures, such as drilling and cone penetrometer, must be avoided.

Ambient noise analysis rests on the assumption that the noise wavefield from 0.5 to 20 Hz is constituted of surface waves, with a minor but significant contribution from body waves (Li *et al.* 1984; Horike 1985). This assumption has been validated by observation and comparison between field measurements and synthetic tests, however the relative proportion of these waves still remains an open issue. Similarly, it is difficult to evaluate with sufficient accuracy the relative contribution of Love and Rayleigh waves (Köhler *et al.* 2007), and among these to establish a precise proportion between fundamental and higher modes (for a complete literature review see Bonnefoy-Claudet *et al.* 2006a). Asten *et al.* (2004) and Asten (2006), with a technique titled multimode SPAC (MMSPAC), specifically recognizes the possibility of the identification of multiple modes. So far, a general agreement is present on the fact that Love waves are in most cases dominant (Okada 2003).

Nevertheless, a certain number of site-dependent controlling factors can be listed: type, orientation and spatial distribution of shallow and buried sources, as well as seismic impedance and attenuation values for the investigated site.

The predominant contribution of surface waves in the noise wavefield is the main property on which several techniques based on single and multistation recording were developed. Among these, the ambient noise horizontal-to-vertical spectral ratio (Nogoshi & Igarashi 1971) is a simple single-station method that has been widely used in the past years to obtain estimations of the fundamental frequency of resonance of soils (f_0). In case of strong velocity contrast between sediments and bedrock, f_0 is close to the first maximum of the Rayleigh ellipticity fundamental mode, most likely always present in the H/V spectrum (e.g. Lachet & Bard 1994; Fäh *et al.* 2003). The simultaneous presence of Love and body waves in the noise wavefield, other than the interaction and superposition of higher modes, makes the identification of the ellipticity function within spectral ratios ambiguous (Fäh *et al.* 2001). In practice, only in certain situations it is possible to separate and extract (with acceptable confidence) the stable portion of that curve. These portions, moreover, can be addressed only to the fundamental mode of propagation, but nothing can be said about higher modes. Several attempts to avoid this problem have been proposed, for example, modelling the whole H/V spectrum by mixing some contributions of Love and Rayleigh waves and including higher modes (Arai & Tokimatsu 2004; Parolai *et al.* 2005). This method has the advantage of not requiring any previous separation of wave components. However, it strictly depends on a certain number of assumptions (e.g. source type and distribution) that are difficult to be verified.

In this paper, we propose a new method to evaluate the Rayleigh-wave modal ellipticity function. We modified a version of the high-resolution frequency–wavenumber analysis proposed by Capon (1969). Our technique rests on the simple fact that the power spectrum calculated with it preserves, along with the phase information, the amplitude characteristics of the investigated signal (Marzetta 1983). Being able to perform this transformation both on the vertical and horizontal radial-polarized directions of motion (Fäh *et al.* 2008) allows us to reconstruct the signal's in-plane particle motion. Thus, for Rayleigh waves, the modal ellipticity function can be directly evaluated by performing the H/V spectral ratios between f–k power amplitudes. Such amplitudes correspond to a specific and well-defined mode of propagation.

With synthetic and real data sets, we demonstrate that this method allows us to obtain, at one time and with the same elaboration scheme, key data about Rayleigh waves: phase velocity dispersion curves and ellipticity. A combined inversion, together with Love wave dispersion or other constraints, might help in decreasing the non-uniqueness of the problem and avoiding solutions that are trapped in local minima (Fäh *et al.* 2008).

2 METHOD

Frequency–wavenumber analysis is a spectral technique based on seismic array recording. Such methods have been widely used in determining earthquake direction, in monitoring nuclear explosions and in estimating wave phase velocity. In particular, high resolution beamforming (Capon 1969), also known as the maximum likelihood or minimum variance method, is a popular data adaptive and alias-free algorithm for computing the frequency–wavenumber spectrum. Applying this method to ambient noise recordings helps us to understand the general composition of the microseismic wavefield: its wave content, propagation and surface wave dispersion.

Since the vertical component of ground motion is affected only by body and Rayleigh wave propagation phenomena (Love component results in an horizontally polarized wavefield), f–k array processing has been employed extensively to derive data on Rayleigh wave phase velocity dispersion (Kind *et al.* 2005; Wathelet 2005). Recent improvements (Fäh *et al.* 2008) allow us to analyse full ground motion (both horizontal and vertical components) to identify and separate the two complementary surface wave contributions. This is done through radial/transversal polarization analysis. In addition, we extended the technique to estimate the signal spectral power content with the goal of evaluating frequency-dependent Rayleigh wave particle motion.

2.1 Basic array processing

Let us consider a spatial configuration of n seismic vertical receivers located at coordinates $[x_1\ x_2\ ...\ x_n,\ y_1\ y_2\ ...\ y_n]$. In the simplest case, this sensor array samples a narrowband planar wavefield $a(f)$ that propagates along the surface from a source located at infinite distance (far-field approximation) in direction θ, also defined as the direction of arrival (DOA). If no attenuation phenomena are assumed, the frequency dependent wavefield amplitude is constant to $|a(f)|$ at each receiver location. However, each sensor samples the plane wave with a certain phase shift depending on its coordinates, the DOA, the analysed frequency f and the wave slowness s. In the frequency domain, the i-esim receiver output can therefore be expressed through its constituents as

$$u_i(f) = g(f)a(f)e^{-2\pi jfs[\cos(\theta)x_i+\sin(\theta)y_i]} \tag{1}$$

or, identically, in terms of wavenumber

$$\begin{aligned} u_i(f) &= g(f)a(f)e^{-2\pi j|\mathbf{k}|[\cos(\theta)x_i+\sin(\theta)y_i]} \\ &= g(f)a(f)e_i(\mathbf{k}). \end{aligned} \tag{2}$$

If we define the 'true' signal steering vector as

$$\mathbf{e}(\mathbf{k}) = [e_1(\mathbf{k})e_2(\mathbf{k})...e_n(\mathbf{k})]^T \tag{3}$$

the receiver output can be expressed in vectorial notation as

$$\mathbf{u}(f) = g(f)a(f)\mathbf{e}(\mathbf{k}). \tag{4}$$

A gain scaling factor $g(f)$ is also included to represent the instrumental amplification of the seismometers. However for simplicity and without any loss of generality, we can set this parameter equal to unity for each station location. Finally, an additional amount of incoherent noise, not addressable to wave propagation phenomena, should be realistically included as a frequency dependent noise vector $\boldsymbol{\eta}(f)$

$$\mathbf{u}(f) = a(f)\mathbf{e}(\mathbf{k}) + \boldsymbol{\eta}(f). \tag{5}$$

Note that the incoherent noise is not related to the 'ambient noise' wavefield, which in this case is the coherent signal to analyse. Such disturbance must be considered the true noise of the system, and should therefore be treated statistically (Strobbia 2003). Incoherent noise can be generated from an ensemble of different sources, that is, non-systematic digitization errors, electrical disturbances or local, uncorrelated microvibrations of the ground. Later we will demonstrate how this variable amount of noise can drastically influence the efficiency of beamforming methods.

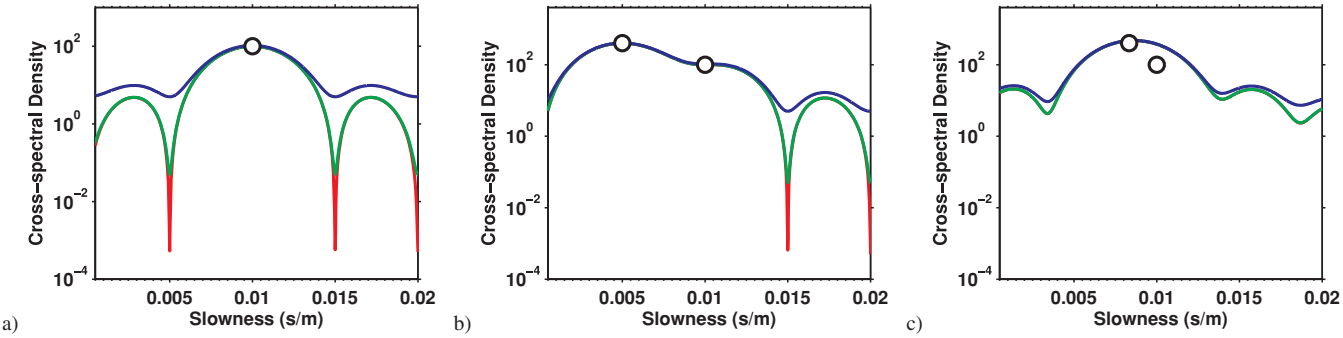

Figure 1. Signal identification using classical beamforming: a linear array of 20 receivers with spacing of 5 m is employed. The power output is calculated for a frequency of 2 Hz and different noise variances are included for comparison (0.1 in red, 1 in green and 10 in blue). In case (a) a single signal with velocity of 100 m s^{-1} and amplitude 10 is analysed. In case (b) two signals with velocities of 100 and 200 m s^{-1} and amplitudes 10 and 20 are considered. In case (c) the two signals of (b) now have a velocity of 100 and 120 m s^{-1}, respectively. True amplitudes are also presented for comparison (black circles).

Under the assumption of uncorrelation between signal and noise, the receiver output vector is then used to estimate the signal cross-correlation (or 'covariance') spectral matrix as

$$\begin{aligned}\hat{\mathbf{R}}(f) &= E\{\mathbf{u}(f)\mathbf{u}^h(f)\} \\ &= E\{\mathbf{e}(\mathbf{k})a(f)a^h(f)\mathbf{e}^h(\mathbf{k})\} + E\{\boldsymbol{\eta}(f)\boldsymbol{\eta}^h(f)\},\end{aligned} \tag{6}$$

where the superscript h denotes conjugate (Hermitian) transpose and E stands for expectation. Note that the products between signal and noise are suppressed because of the uncorrelation. In practice, the expected value is obtained from an average between several cross-correlation snapshots of successive time-windows (block averaging).

At a specific frequency, we can assume the noise of the system to be a zero mean Gaussian process with variance $\sigma^2(f)$. Therefore, for a stationary signal the eq. (6) simplifies to

$$\hat{\mathbf{R}}(f) = \mathbf{e}(\mathbf{k})|a(f)|^2\mathbf{e}^h(\mathbf{k}) + \sigma^2(f)\hat{\mathbf{I}}, \tag{7}$$

where $\hat{\mathbf{I}}$ is the identity matrix. From the cross-correlation matrix, the 'total array power output' $P(f)$ can then be calculated by summing its elements

$$P(f) = [\mathbf{1}]^h\hat{\mathbf{R}}(f)[\mathbf{1}], \tag{8}$$

where $[\mathbf{1}]$ is a vector of n elements equal to 1.

2.2 Classical beamforming

In classical beamforming techniques (Lacoss *et al.* 1969), the total array power output is weighted with a filter vector $\mathbf{w}(\mathbf{k})$ equal to the 'presumed' signal steering vector $\mathbf{e}_p(\mathbf{k})$ divided by the number of sensors

$$P(f, \mathbf{k}) = \mathbf{w}^h(\mathbf{k})\hat{\mathbf{R}}(f)\mathbf{w}(\mathbf{k}), \tag{9}$$

$$\mathbf{w}(\mathbf{k}) = \frac{\mathbf{e}_p(\mathbf{k})}{n}. \tag{10}$$

The true signal steering vector is initially unknown, as are the direction of propagation and the velocity of the investigated wave. However, identifying the correct value is straightforward; a direct grid search over s and θ (or identically over k_x and k_y) can be performed. The presumed steering vector is thus rebuilt every time for each combination of parameters. As a consequence, a maximum in the total array output function is achieved when the presumed and the true steering direction match $[\mathbf{e}_p(\mathbf{k}) = \mathbf{e}(\mathbf{k})]$. In such case is

$$\mathbf{e}_p^h(\mathbf{k})\mathbf{e}(\mathbf{k}) = \mathbf{e}^h(\mathbf{k})\mathbf{e}_p(\mathbf{k}) = n \tag{11}$$

and then for simple substitution in eqs (7), (9) and (10)

$$\begin{aligned}P(f, \mathbf{k}) &= \frac{1}{n^2}\left\{n|a(f)|^2 n + \sigma^2(f)n\right\} \\ &= |a(f)|^2 + \frac{\sigma^2(f)}{n}.\end{aligned} \tag{12}$$

Thus, the array power output corresponds to the true energy of the signal, plus an amount of distortion introduced by the noise variance (Fig. 1a).

As shown, this approach preserves the amplitude characteristics in cases of minimum or null noise variance (or a large number of receivers) and when a perfect match holds between the true and the presumed steering vectors. Unfortunately, it is not robust enough to sufficiently minimize the power output in a situation of progressive steering vectors mismatch. That case results in a generally poor resolution and can be summarized by analysis of the theoretical array response or 'beampattern'. This represents the array power output for a signal of unitary amplitude and zero phase (e.g. the case of a vertically incident plane wave).

$$B(\mathbf{k}) = \mathbf{w}^h(\mathbf{k})[\hat{\mathbf{1}}]\mathbf{w}(\mathbf{k}). \tag{13}$$

Here $[\hat{\mathbf{1}}]$ is a square matrix of $n \cdot n$ elements equal to 1. The array power output for any generic wavefield can be obtained by convolving the theoretical response with the signal impulse in the wavenumber domain (Wathelet 2005). It is therefore evident that the shape of the beampattern function will be the primary factor in controlling the resolution.

Furthermore, any assumption of a wavefield constituted by only a single plane wave cannot realistically represent ambient noise phenomena. In real situations multiple signals propagate simultaneously, impinge the array from different directions and overlap one another. Let us consider, as an example, the propagation of M surface wave higher modes

$$\mathbf{u}(f) = \sum_{i=1}^{M} a_i(f)\mathbf{e}(\mathbf{k}_i) + \boldsymbol{\eta}(f). \tag{14}$$

Following from eq. (6) and under the assumption that the noise and the signals are uncorrelated, the cross-correlation matrix has the form

$$\hat{\mathbf{R}}(f) = E\left\{\sum_{i=1}^{M}\sum_{l=1}^{M}\mathbf{e}(\mathbf{k}_i)a_i(f)a_l^h(f)\mathbf{e}^h(\mathbf{k}_l)\right\} + \sigma^2(f)\hat{\mathbf{I}}. \tag{15}$$

However, in case of ambient noise, we can assume the signals are non-stationary over long durations. Consequently, different signals

($i \neq l$) can be reasonably considered to be uncorrelated over successive time window snapshots. In such a case, the mixed products of the previous equation tend to vanish by means of the expectation procedure. Therefore the cross-correlation matrix simplifies to

$$\hat{\mathbf{R}}(f) \simeq \sum_{i=1}^{M} \mathbf{e}(\mathbf{k}_i)|a_i(f)|^2\mathbf{e}^h(\mathbf{k}_i) + \sigma^2(f)\hat{\mathbf{I}}. \tag{16}$$

It is easy to demonstrate that the total power output is distorted by the reciprocal interference between wavefields as well as noise. As in the previous example, once the steering vector of the signal of interest is identified [e.g. $\mathbf{e}_p(\mathbf{k}) = \mathbf{e}(\mathbf{k}_1)$], the corresponding amplitude will deteriorate due to the M interfering steering vectors

$$\begin{aligned} P(f, \mathbf{k}_1) \simeq\ & |a_1(f)|^2 \\ & + \sum_{i=2}^{M} \frac{|a_i(f)|^2}{n^2}\mathbf{e}^h(\mathbf{k}_1)\mathbf{e}(\mathbf{k}_i)\mathbf{e}^h(\mathbf{k}_i)\mathbf{e}(\mathbf{k}_1) \\ & + \frac{\sigma^2(f)}{n}. \end{aligned} \tag{17}$$

Nevertheless, this amplitude approximation has been experimentally demonstrated to be valid if the signals are not too similar (in terms of DOA and slowness, e.g. Figs 1b and c) and the number of receivers is sufficiently large to minimize the beampattern geometry effect (Asten & Henstridge 1984). Note as well that the noise variance influences the total power output $P(f, \mathbf{k})$ as a positive amplitude shift of the power spectrum only. Its shape will remain unmodified.

2.3 High resolution beamforming

In high resolution beamforming, the target is to weight the array power output with a 'data adaptive' filter vector $\mathbf{w}(\mathbf{k})$. This minimizes distortions induced by mismatches between the true and the presumed steering vector, and at the same time minimizes the influence of uncorrelated noise (Capon 1969; Marzetta 1983). However, the procedure should not affect the signal correlation in the final result. In practice, we want to solve the following quadratic minimization problem:

$$P(f, \mathbf{k}) = \min_{\mathbf{w}} \left\{\mathbf{w}^h(\mathbf{k})\hat{\mathbf{R}}(f)\mathbf{w}(\mathbf{k})\right\} \tag{18}$$

subject to the amplitude constraint

$$\mathbf{w}^h(\mathbf{k})\mathbf{e}_p(\mathbf{k}) = 1. \tag{19}$$

The minimization problem can be solved using the Lagrange multiplier in this form

$$\mathbf{w}(\mathbf{k}) = \frac{\hat{\mathbf{R}}^{-1}(f)\mathbf{e}_p(\mathbf{k})}{\mathbf{e}_p^h(\mathbf{k})\hat{\mathbf{R}}^{-1}(f)\mathbf{e}_p(\mathbf{k})}. \tag{20}$$

Consequently, the weighted power output (18) will be expressed for substitution and resulting simplification as

$$P(f, \mathbf{k}) = \frac{1}{\mathbf{e}_p^h(\mathbf{k})\hat{\mathbf{R}}^{-1}(f)\mathbf{e}_p(\mathbf{k})}. \tag{21}$$

As in the case of classical beamforming, the true signal steering vector can be found with a simple grid search over s and θ. In addition, we now want to evaluate to what degree the total power output can deviate from the true energy of the signal when a perfect match occurs between the true and presumed steering vector. To analyse this we use a singular value decomposition. The steering vector can be factorized into its orthonormal basis ($\hat{\mathbf{J}}$ and L) and singular values ($\mathbf{K}$) as

$$\mathbf{e}(\mathbf{k}) = \hat{\mathbf{J}}\mathbf{K}L^h, \tag{22}$$

where $\hat{\mathbf{J}}$ is a $n \cdot n$ orthogonal matrix containing the basis vector directions of $\mathbf{e}(\mathbf{k})$ and L is a scalar with the only admissible values ± 1. The decomposition of a steering vector always produces one unique singular value. Consequently, $\mathbf{K}$ is a column vector with all elements, except the first, equal to 0. Similarly, for the steering vector cross-product, an Hermitian positive semi-definite matrix, it is always possible to find an eigendecomposition that satisfies

$$\mathbf{e}(\mathbf{k})\mathbf{e}^h(\mathbf{k}) = \hat{\mathbf{J}}\mathbf{K}L^hL\mathbf{K}^h\hat{\mathbf{J}}^h = \hat{\mathbf{J}}\hat{\mathbf{S}}\hat{\mathbf{J}}^h, \tag{23}$$

where $\hat{\mathbf{S}}$ is the $n \cdot n$ diagonal eigenvalue matrix. Summarizing, the following relations are then valid

$$\begin{aligned} L &= \pm 1, \\ \mathbf{K}\mathbf{K}^h &= \hat{\mathbf{S}}, \\ \hat{\mathbf{J}}\hat{\mathbf{J}}^h &= \hat{\mathbf{J}}^h\hat{\mathbf{J}} = \hat{\mathbf{I}}. \end{aligned} \tag{24}$$

Given the decomposition in (23), we have the property

$$tr(\mathbf{e}(\mathbf{k})\mathbf{e}^h(\mathbf{k})) = tr(\hat{\mathbf{S}}) = tr(\mathbf{K}\mathbf{K}^h) = n, \tag{25}$$

where tr stands for matrix trace. Therefore, the unique singular value in $\mathbf{K}$ will be exactly $\sqrt{n}$.

The inverse of the cross-correlation matrix of eq. (7) can then be expressed for substitution as

$$\hat{\mathbf{R}}^{-1}(f) = \left\{|a(f)|^2\hat{\mathbf{J}}\hat{\mathbf{S}}\hat{\mathbf{J}}^h + \sigma^2(f)\hat{\mathbf{I}}\right\}^{-1}, \tag{26}$$

$$\hat{\mathbf{R}}^{-1}(f) = \frac{1}{|a(f)|^2}\left\{\hat{\mathbf{J}}\hat{\mathbf{S}}\hat{\mathbf{J}}^h + \frac{\sigma^2(f)}{|a(f)|^2}\hat{\mathbf{I}}\right\}^{-1}. \tag{27}$$

Because $\hat{\mathbf{J}}$ is orthogonal and consequently $\hat{\mathbf{J}}\hat{\mathbf{J}}^h = \hat{\mathbf{I}}$, it is possible to write

$$\hat{\mathbf{R}}^{-1}(f) = \frac{1}{|a(f)|^2}\left\{\hat{\mathbf{J}}\hat{\mathbf{S}}\hat{\mathbf{J}}^h + \hat{\mathbf{J}}\frac{\sigma^2(f)}{|a(f)|^2}\hat{\mathbf{I}}\hat{\mathbf{J}}^h\right\}^{-1} \tag{28}$$

and using the distributive property of matrix multiplication

$$\hat{\mathbf{R}}^{-1}(f) = \frac{1}{|a(f)|^2}\left\{\hat{\mathbf{J}}\left\{\hat{\mathbf{S}} + \frac{\sigma^2(f)}{|a(f)|^2}\hat{\mathbf{I}}\right\}\hat{\mathbf{J}}^h\right\}^{-1}. \tag{29}$$

From the property $\{\hat{\mathbf{A}}\hat{\mathbf{B}}\hat{\mathbf{C}}\}^{-1} = \hat{\mathbf{C}}^{-1}\hat{\mathbf{B}}^{-1}\hat{\mathbf{A}}^{-1}$ it follows that

$$\hat{\mathbf{R}}^{-1}(f) = \frac{1}{|a(f)|^2}\{\hat{\mathbf{J}}^h\}^{-1}\left\{\hat{\mathbf{S}} + \frac{\sigma^2(f)}{|a(f)|^2}\hat{\mathbf{I}}\right\}^{-1}\{\hat{\mathbf{J}}\}^{-1} \tag{30}$$

and because $\{\hat{\mathbf{J}}^h\}^{-1} = \hat{\mathbf{J}}$ and identically $\hat{\mathbf{J}}^{-1} = \hat{\mathbf{J}}^h$ we obtain

$$\hat{\mathbf{R}}^{-1}(f) = \frac{1}{|a(f)|^2}\hat{\mathbf{J}}\left\{\hat{\mathbf{S}} + \frac{\sigma^2(f)}{|a(f)|^2}\hat{\mathbf{I}}\right\}^{-1}\hat{\mathbf{J}}^h. \tag{31}$$

Consequently, using the decomposition in eqs (22), the total power output in (21) can be expressed as

$$P(f, \mathbf{k}) = \frac{|a(f)|^2}{L\mathbf{K}^h\hat{\mathbf{J}}^h\hat{\mathbf{J}}\left\{\hat{\mathbf{S}} + \frac{\sigma^2(f)}{|a(f)|^2}\hat{\mathbf{I}}\right\}^{-1}\hat{\mathbf{J}}^h\hat{\mathbf{J}}\mathbf{K}L^h}, \tag{32}$$

and using the properties in (24)

$$P(f, \mathbf{k}) = \frac{|a(f)|^2}{\mathbf{K}^h\left\{\mathbf{K}\mathbf{K}^h + \frac{\sigma^2(f)}{|a(f)|^2}\hat{\mathbf{I}}\right\}^{-1}\mathbf{K}}. \tag{33}$$

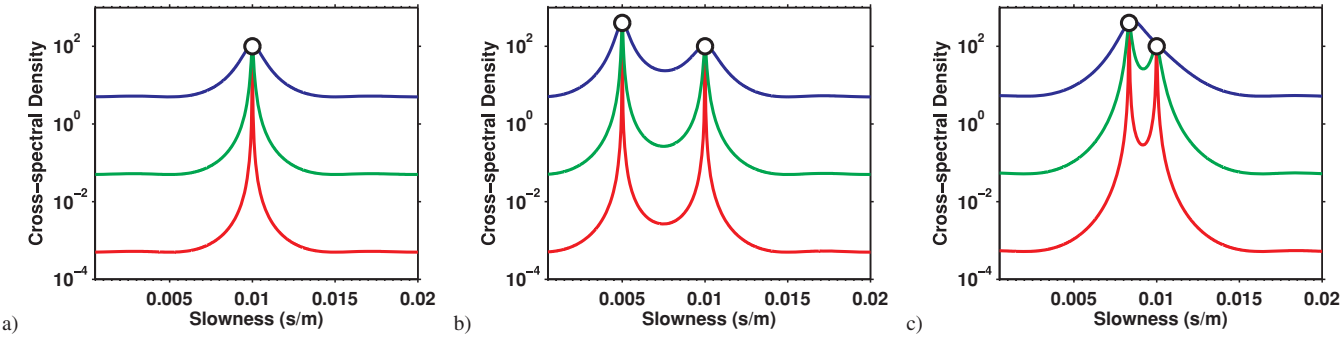

Figure 2. Signal identification using high-resolution beamforming: we use the same array configuration as in Fig. 1. Compared to classical beamforming, this method allows more accurate identification of single (a) and multiple signals (b), minimizing the effect of the array response. As evident using the three previous noise variances, the total power output level is sensitive to the amount of uncorrelated noise. In case of strong noise variance (blue line), if two signals are too close in slowness (case c) even this method will fail, giving rise to artefact peaks.

Therefore, given the characteristics of $\mathbf{K}$ obtained from the considerations in (25), the previous equation simplifies to a purely scalar form

$$P(f,\mathbf{k}) = \frac{|a(f)|^2}{\left\{\frac{n|a(f)|^2}{n|a(f)|^2+\sigma^2(f)}\right\}} = \left\{|a(f)|^2 + \frac{\sigma^2(f)}{n}\right\}. \quad (34)$$

As in classical beamforming, if the noise variance is assumed to be small and/or the number of receivers is sufficiently large, this technique can closely reconstruct the original power amplitude with only negligible distortion (Fig. 2a). Note, however, that if the noise variance is too small or even zero, the method cannot be applied. In this case, the signal cross-correlation matrix is singular or close to singularity and consequently cannot be inverted. In such situations it is common practice to introduce some artificial noise to the system using a matrix diagonal load (Capon 1969). This procedure stabilizes the inversion, but has the disadvantage of depending on the defined optimal load being applied without considerable signal distortion. Asten (1976) has experimentally investigated the phenomena and proposed a percentual loading value of 1.02 with no significant loss in resolution.

The case of multiple signals is not straightforward to demonstrate mathematically, but has been experimentally investigated. Using synthetic signals, we observe that the performance of high-resolution beamforming is still superior to the classic method whenever the steering vector of the signal of interest is identified (Fig. 2b). However, the amplitude dependence on noise variance, steering vector mismatching and signal interference is no longer linear. In general, incoherent noise most strongly influences the shape of the total power spectrum (Asten & Henstridge 1984). Consider the simultaneous presence of two signals coming from the same direction with only slightly different velocities, as for two surface wave higher modes whose dispersion curves are close to apparent intersection. In such situations, if the incoherent noise within the system is large, correctly identifying the signal velocities is impossible (Fig. 2c, blue line), because the adaptive filter is not able to resolve the two contributions separately. Consequently, the corresponding amplitude maxima tend to converge or even merge, giving the impression of a unique signal of average characteristics. The amplitude of this resultant maximum no longer represents one of the original signals. In such a situation, the definition of a general rule that explains at which point the method will fail is not an easy task. Other than on the noise variance of the system, the resolution depends on frequency, on the number of receivers, their configuration and on the relative amplitude of the signals. Note, however, that the true amplitudes are still preserved at their correct locations. This last point is of fundamental importance because, if the correct velocity is identified in some way (e.g. through a procedure of noise filtering), then the true amplitude, or a good approximation thereof, can be obtained.

2.4 Noise filtering and diagonal loading

We use a hybrid singular-value-decomposition approach that combines noise filtering and loading to improve the resolution of the method. Note that for a number of coherent signals smaller than the number of seismic receivers, the smallest singular value of the matrix $\hat{\mathbf{R}}$ approximates the uncorrelated noise variance σ^2 of the system (Kogon 2003). Even for a higher number of signals, this approximation is, in most cases, still valid. Based on this assumption, we can hypothetically remove the influence of noise by subtracting this value from each singular value of the signal cross-correlation matrix. In this case, however, the matrix of singular values becomes rank deficient (its last element is equal to 0) and thus $\hat{\mathbf{R}}$ is no longer invertible. We have then two possibilities: the first is to use a Moore-Penrose pseudo-inversion that cuts out the null space from the covariance matrix and produce a least squares solution (Sibul 1984). The second option consists, by contrast, of loading the singular values of $\hat{\mathbf{R}}$ with a small quantity to make the matrix of singular values artificially full rank. In this second case, unfortunately, identifying the optimum amount of load to apply is not obvious. However, some general rules can be defined: obviously, the final amount of load must be less than the filtered noise variance, by at least one or two orders of magnitude, but must be sufficiently large to be numerically invertible, depending on the characteristics of the software used.

This last approach, theoretically more suitable because it produces sharp maxima in the spectrum, in practice can lead to an undervaluation of amplitudes. This happens with a sampling of the grid search over the slowness–azimuth plane that is too coarse (Asten & Henstridge 1984). If the signal peak becomes too sharp and is localized between two consecutive samples, it cannot be correctly identified. In contrast, the first approach, based on pseudo-inversion, better preserves the amplitude information but tends toward erroneous localization of maxima. As a direct consequence, we implement a two-step approach: first using a filtering+loading scheme to correctly localize the signal in the slowness–azimuth plane, and then computing the correct amplitude value at the retrieved location with a pseudo-inversion approach.

2.5 Three component *f –k* spectrum

Three component *f–k* analysis (Fäh *et al.* 2008) extends the original high-resolution algorithm. This is based on the assumption that the superimposed contribution of Love and Rayleigh waves over the horizontal component of motion can be separated with a DOA decomposition. The horizontal component cross-power spectral matrix is in this case azimuth dependent. Thus, it must be recalculated for each possible direction-of-polarization θ (DOP) as a combination of the north–south and east–west ground motions

$$\mathbf{u}_H(f,\theta) = \mathbf{u}_{NS}(f)\cos(\theta) + \mathbf{u}_{EW}(f)\sin(\theta), \tag{35}$$

$$\hat{\mathbf{R}}_H(f,\theta) = E\{\mathbf{u}_H(f,\theta)\mathbf{u}_H^h(f,\theta)\}. \tag{36}$$

The array power output is therefore generated separately for Rayleigh waves (the radial part) as a result of all in-phase contributions with DOA equal to the DOP

$$P_H^R(f,s,\theta) = \frac{1}{\mathbf{e}_p^h(s,\theta)\hat{\mathbf{R}}_H^{-1}(f,\theta)\mathbf{e}_p(s,\theta)}. \tag{37}$$

For Love waves (the transversal part) as a result of all in-phase contributions with DOA orthogonal to DOP

$$P_H^L(f,s,\theta) = \frac{1}{\mathbf{e}_p^h(s,\theta)\hat{\mathbf{R}}_H^{-1}(f,\theta+\frac{\pi}{2})\mathbf{e}_p(s,\theta)}. \tag{38}$$

All previous considerations regarding the amplitude characteristics of the vertical component of motion are thus valid for processing of the two horizontal components.

2.6 Rayleigh ellipticity function evaluation

Now we focus on the relation between the amplitude characteristics of spectra calculated for both the horizontal-radial and the vertical components of motion. As previously shown, the Capon algorithm allows us to reconstruct a signal's power content whenever its true location is correctly identified in the $s-\theta$ plane. If multiple signals are simultaneously present in the wavefield (e.g. several modes of propagation of surface waves), the method can at least theoretically identify and separate the energy content of each contribution (Marzetta 1983). Thus, we can demonstrate that for a signal corresponding to a specific Rayleigh wave mode, the amplitude ratio between the horizontal-radial (eq. 37) and the vertical *f–k* spectra (eq. 21) will also represent its Rayleigh mode-related ellipticity function. Obviously, the square root of the ratio should be considered, because cross-correlation methods provide an estimation of energy, whereas ellipticity is usually represented in terms of displacement.

$$ell_{H/V}^R \simeq \frac{\sqrt{P_H^R(f,s,\theta)}}{\sqrt{P_V^R(f,s,\theta)}} = \sqrt{\frac{\mathbf{e}_p^h(s,\theta)\hat{\mathbf{R}}_V^{-1}(f)\,\mathbf{e}_p(s,\theta)}{\mathbf{e}_p^h(s,\theta)\hat{\mathbf{R}}_H^{-1}(f,\theta)\,\mathbf{e}_p(s,\theta)}}. \tag{39}$$

Clearly, to avoid numerical scaling errors, the two spectral components must be processed with the same scheme of parametrization (windowing length, tapering type, gain, etc.).

However, as we have already stressed, ambient noise can be considered as an ensemble of several signals generated from sources uniformly distributed around the array. In this context, wave packets that belong to the same mode of propagation can exist with very different absolute amplitude, depending on the source distance, type, orientation and intensity. Consequently, to retrieve true ellipticity, we must perform the spectral ratio between picked maxima that belong exclusively to the same signal on the horizontal-radial and vertical components. In this way, any scaling factor induced by source variability is automatically removed by the ratio.

Figs 3(a1) and (b1) shows an example of maxima localization in the slowness–azimuth planes. Two modes of propagation are clearly identifiable and several signals that belong to these modes are picked up from different directions of arrival. Note that identifying these maxima is separate for the horizontal-radial and vertical components of motion. This approach is necessary because the energy carried by Rayleigh waves could drastically vary between the two, or even vanish in certain frequency ranges (Fig. 4). Thus, there could be signals that can be identified only in a specific direction of motion. This is common for the frequency range corresponding to the fundamental mode ellipticity first maxima, where the vertical displacement always decreases toward zero. Consequently, once a mode is identified on one component, the corresponding amplitude value in the complementary direction is also extracted. Then the ratio is performed (Fig. 5).

Finally, the ensemble of all picked values from both components of motion (Fig. 6a) is analysed statistically by using a normalized probability density distribution. From the histogram representation (Fig. 6b), the expected values of ellipticity are then manually extracted for each frequency.

2.7 Resolution capabilities

In classical beamforming techniques and partially in Capon's method, theoretical spectral resolution is controlled by the kind of temporal and spatial sampling that the sensor array performs on the seismic wavefield. Since the temporal sampling is always uniform and generally very dense, simple rules such as the 'Nyquist–Shannon' theorem can be applied to define the corresponding frequency resolution limits. In most cases these cover an extremely broad range

$$f_{\min} = \frac{1}{T}, \tag{40}$$

$$f_{\max(\text{Nyquist})} = \frac{1}{2\mathrm{d}t}, \tag{41}$$

where dt is the temporal sampling rate and T is the total duration of the record.

By contrast, the receiver spatial configuration is commonly very irregular, since practical obstacles (e.g. buildings inside a city) can force a non-optimal sensor location. Moreover, the number of available seismic detectors is drastically limited by cost. As a direct consequence, special considerations are necessary to reconstruct the correct signal amplitude.

To define the wavenumber resolution limits of beamforming methods, we express the theoretical array response of eq. (13) in index notation (Wathelet *et al.* 2008) as

$$\begin{aligned} B(\mathbf{k}) &= \frac{1}{n^2}\sum_{i=1}^{n}\sum_{l=1}^{n} e^{-j[k_x(x_i-x_l)+k_y(y_i-y_l)]} \\ &= \left|\frac{1}{n}\sum_{i=1}^{n} e^{-j(k_x x_i + k_y y_i)}\right|^2. \end{aligned} \tag{42}$$

Note that the beampattern function can also be expressed as the squared impulse response of the bidimensional discrete Fourier transform, whose periodicity imposes a wavenumber aliasing limit

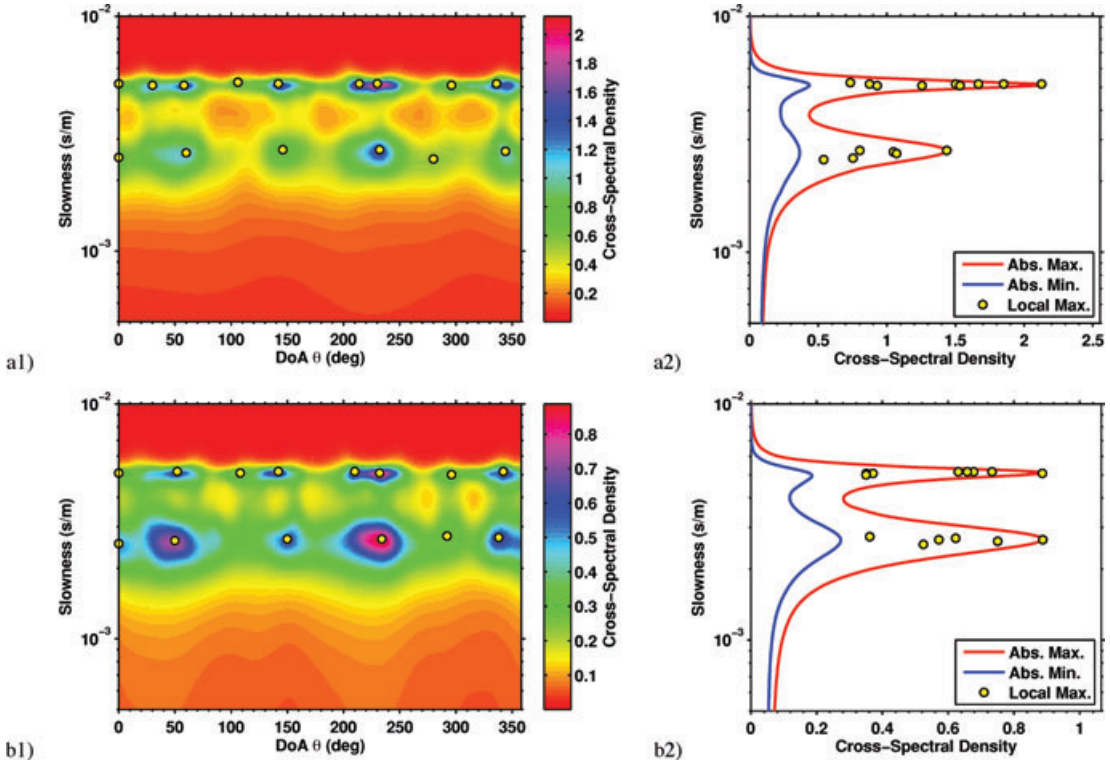

Figure 3. Example of three-component f–k processing using synthetic noise data (see SESAME model M2.2 described in paragraph 3.1, with array geometry given by the ensemble of all 39 receivers of Fig. 7). Identifying multiple signals on the slowness–azimuth plane is performed separately for the vertical (a1, a2) and the horizontal-radial (b1, b2) components and for each frequency (an example given here at 8 Hz) using an automatic procedure. It can be observed that the local maxima picked at a specific slowness value (yellow dots) may have different amplitudes within the range of the minimum and maximum cross-power spectrum along azimuth (Abs. Min. and Abs. Max. in a2, b2). Their localization, however, clearly indicate the existence of two separate modes of propagation.

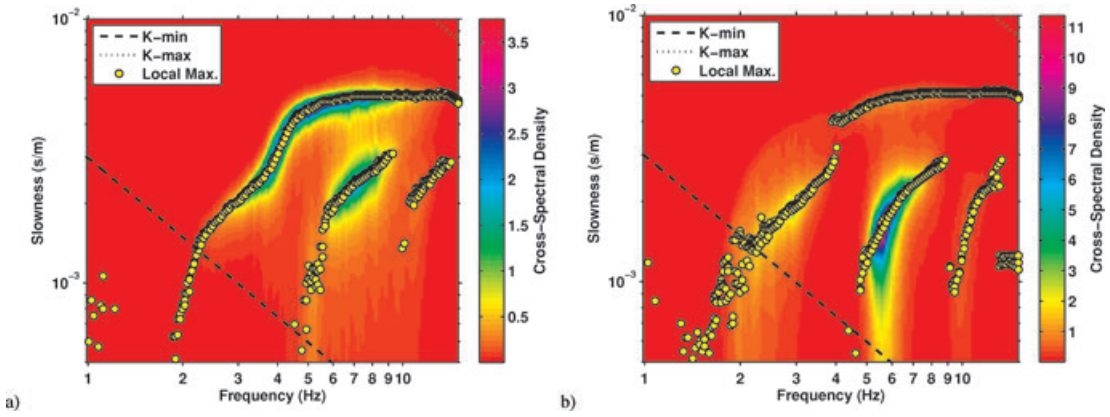

Figure 4. Following the example of Fig. 3, all the maxima picked on the slowness–azimuth planes at different frequencies are then collected on the corresponding slowness–frequency planes (a, for vertical and b, for horizontal radial component) to extract the modal dispersion curves. The surface of maximum cross-power along azimuth is also presented in background for comparison. It is interesting to note that even if the modal dispersion curves are comparable between the two components, the distribution of energy is different. Minimum ($k_{\min}$) and maximum ($k_{\max}$) wavenumber resolution limits are defined as in Section 2.7.

of

$$|\mathbf{k}|_{\max} = \frac{1}{2D_{\min}}, \tag{43}$$

where $D_{\min}$ is the minimum distance between receivers within the array. With some limitations, however, we observed that some results can also be obtained with the high-resolution method in the range

$$\frac{1}{2D_{\min}} \leq |\mathbf{k}| \leq \frac{1}{D_{\min}} \tag{44}$$

due to partial suppression of aliasing induced by adaptive filtering. Clearly, in this extended range, the number of available receivers most strongly influences the quality of achievable results.

Defining the wavenumber lower resolution bound is a matter of discussion (Tokimatsu 1997; Park *et al.* 1999). We proceed then on the basis of the following. By substitution of variables, eq. (42) can also be expressed in the form

$$B(\mathbf{k}) = \frac{1}{m}\sum_{s=1}^{m} e^{-j(k_x X_s + k_y Y_s)}, \tag{45}$$

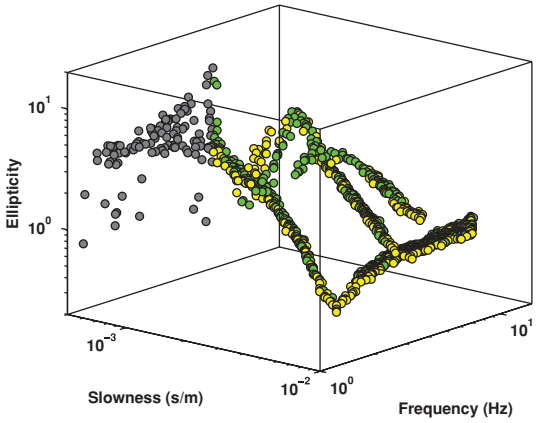

Figure 5. Representing the selected ellipticity values in three dimensions helps to identify and isolate clusters of points that belong to the same mode of propagation. This minimizes errors induced by misinterpreting modal jumps and aliasing. The figure presents in green the ellipticity values from signals chosen on the horizontal component only, in yellow those from the vertical and in grey those points beyond resolution limits.

where $m = n^2$ and $[X_s, Y_s] = [x_j - x_l, y_j - y_l]$ are the coordinates of the new transformed domain (the *lag* domain, see Haubrich 1968 for clarification). Note then that the minimum wavenumber will be controlled by the maximum distance $L_{\max}$ between samples in this domain which corresponds to double the maximum existing distance $D_{\max}$ between sensors

$$|\mathbf{k}|_{\min} = \frac{1}{L_{\max}} = \frac{1}{2D_{\max}}. \tag{46}$$

Capon's method improves the resolution range at lower wavenumbers. In the pure theoretical case, without any noise influence, the resolution is infinite (Woods & Lintz 1973). In practice, rather than the array geometry, the level of incoherent noise is the main factor controlling this lower bound. With microtremors, however, an objective estimation of this influence is not straightforward. Consequently, to avoid bias in evaluating the ellipticity function, we decided to be conservative, using the lower limit imposed by classical f–k analysis.

These considerations are theoretically valid for uniform sampling. Nevertheless, given the array's irregular geometry in the two spatial directions, the true resolution becomes azimuth dependent (Zywicki 1999). Several high-amplitude side-lobes in the beampattern can interfere with the signal of interest. However, under the assumption that ambient noise sources are equally distributed around the array, the resolution limits we defined can be considered valid as an upper bound of possibilities.

Additionally, consider the energy content of the signal. Even in the best experimental conditions and inside the resolution limits, if the wave energy is too low, identifying the correct propagation mode is difficult and maxima are hardly visible in the slowness–azimuth plane. Therefore, as an additional resolution constraint, we introduce the following empirical rule: compare only those portions of dispersion curves simultaneously identifiable on both the horizontal and vertical s–f planes.

3 RESULTS

The proposed method has been tested with synthetic and real data sets of ambient noise array recordings. For synthetics, three different models were employed. To make the results comparable, these models were selected with similar ellipticity patterns but with increasing structural complexity, going from a simple layer over a half space to a multilayered model. In contrast, the real case experiment has been conducted blindly. The experiment location, however, was selected to approximate the best experimental conditions.

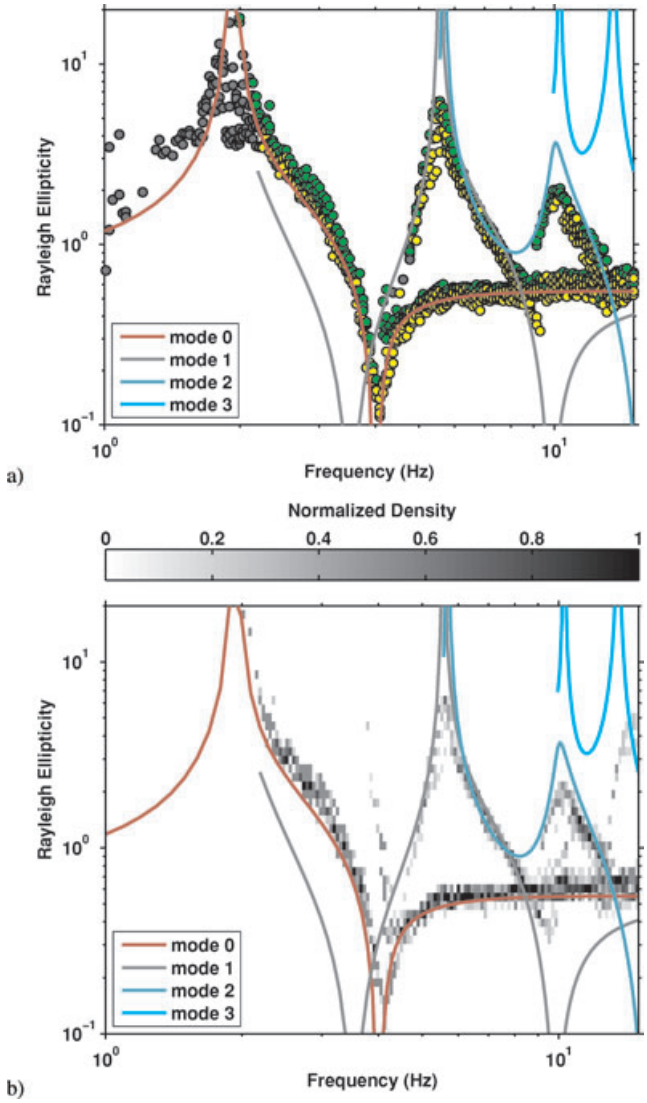

Figure 6. The ensemble of all the calculated ellipticity values from the elaboration of both vertical and horizontal-radial components (a: colors as for Fig. 5) is then statistically analysed. We used a histogram representation (b) to identify a final average value (manually extracted). To make the statistics comparable over different frequencies, the probability density distributions are normalized to their maximum value. Theoretical ellipticities are also presented for comparison (solid curves).

For each processed data set, information about array geometry and resolution, phase velocity dispersion and f–k ellipticity is provided. For synthetics, experimental curves are compared with the corresponding theoretical ones; for real cases, the results from the proposed method are presented together with H/V curves obtained from standard single-station analysis to show the improvement achieved.

For processing synthetic and real data sets, ellipticity and dispersion curves were extracted manually from f–k spectra using the histogram representation presented in Fig. 6(b); manual selection allows a more accurate control over the final result than an automatic

Table 1. Parameters of the 1-D models employed to generate ambient noise synthetics.

	h (m)	V_p (m s^{-1})	V_s (m s^{-1})	ρ (kg m^{-3})	Q_p	Q_s
M2.1	25	500	200	1900	50	25
		2000	1000	2500	100	50
M2.2	25	1350	200	1900	50	25
		2000	1000	2500	100	50
M10.2	18	1350	250	1900	50	25
	18	1350	333	1900	50	25
		2000	1000	2500	100	50
M11.2	4	1350	380	1900	50	25
	4	1350	360	1900	50	25
	4	1350	340	1900	50	25
	4	1350	320	1900	50	25
	4	1350	300	1900	50	25
	4	1350	280	1900	50	25
	4	1350	260	1900	50	25
	4	1350	240	1900	50	25
	4	1350	220	1900	50	25
		2000	1000	2500	100	50

detection procedure. It usually avoids misinterpretation induced by aliasing or modal jumps.

3.1 Synthetic data sets

Synthetics data sets employed to test the method were produced within the *SESAME* European Project ('Site Effects Assessment Using Ambient Vibrations', Deliverable 2004 September 12; Bonnefoy-Claudet *et al.* 2006b) using a modified version of the spectral element modelling code proposed by Hisada (1994). All structural models are 1-D (one or more horizontal soft layers of different thickness over a stiff half space, Table 1). To realistically simulate the behaviour of a sedimentary basin, the layer's velocity (V_p and V_s), density (ρ) and quality factors (Q_p and Q_s) are set to increase at the bedrock interface. Inside the basin low-velocity zones are also permitted. The noise field is forced to represent a source distribution statistically uniform in space and time (for details see SESAME deliverable D12.09-Wp09 'Simulation of seismic noise'). Two different types of source time-functions were employed simultaneously to model the behaviour of the expected ambient noise sources: a delta-like impulse and an harmonic wavelet-type function. Point force orientation is allowed to vary (horizontally and vertically) among sources to give rise to both *P-SV* and *SH* wave propagation phenomena.

Each synthetic data set consist of 39 three-components records calculated for different station locations; each trace is approximately 405 s long. To test the method under the best experimental conditions, we first used all stations simultaneously to extract dispersion and ellipticity curves. However, employing such a huge number of receivers is not realistic, given the high cost of instrumentation. For this kind of survey, the number of acquisition units usually runs between 8 and 16. Therefore, we decided to additionally test small configurations of 13 and 14 stations (Fig. 7). We selected the relative array geometry from the available station locations and tried to resolve the frequency range between 2 and 15 Hz.

3.1.1 Model M2.1

Model M2.1 represents the simplest situation in which a unique horizontal sedimentary layer overlays a high-velocity half-space (the geophysical bedrock). In this case, a unique strong contrast of impedance holds for *S*- and *P*-wave velocities.

For the fundamental mode, using the entire set of available stations, we can obtain a nearly perfect match between the theoretical and experimental ellipticities over the entire frequency range inside the resolution limits of this configuration (Fig. 8a2). A slight overestimation is observed in the middle part of the right flank of the curve; most probably due to the fact that array analysis can minimize the body wave influence, but not entirely remove it. Thus, overestimation can be interpreted as the residual presence of *SH* waves on the horizontal component.

For the first higher mode, good results are obtained only in the frequency range where the corresponding dispersion curve is clearly identifiable in the slowness–frequency plane. In this case, the energy content of the mode is sufficiently large, especially on the horizontal-radial component, and the peak in the ellipticity curve is consequently well defined. For the second higher mode, however, analysis is not straightforward. Only a small portion of the dispersion curve is clearly visible in a range between 9 and 12 Hz and, from the observation of the theoretical curves, the strong influence of the third mode makes the picked maxima deviate from their true location to lower slowness values. This effect reflects on ellipticity, which shows a good amplitude match only in a limited portion.

If we decrease the number of receivers, the analysis is more complex. Using configuration 'selection 1' allows us to obtain the correct value of ellipticity for the fundamental mode only (Fig. 8b2). Nothing can be said for higher modes that are no longer clearly identifiable in terms of dispersion. 'Selection 2' gives better results

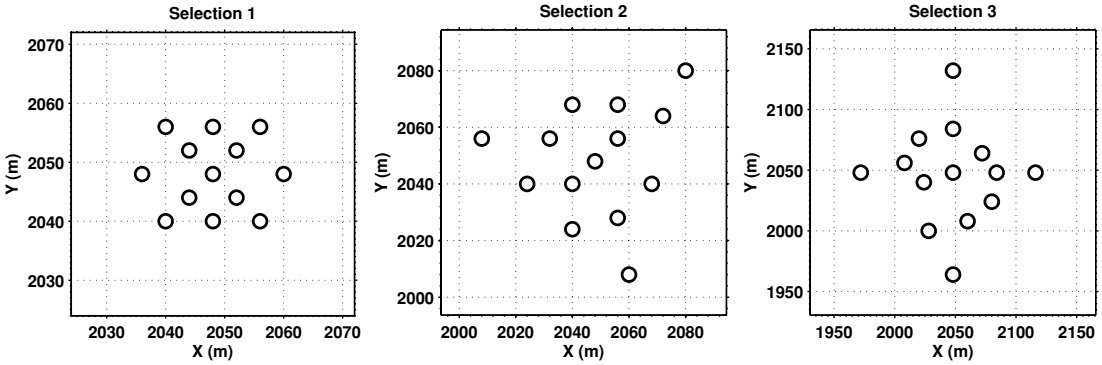

Figure 7. Selected receiver configurations we used for the synthetic tests M2.1, M2.2, M10.2 and M11.2. The three subarrays share the same central station, but the diameter increases progressively from 'selection 1 to 3'. An additional configuration was considered, using all the available 39 receivers.

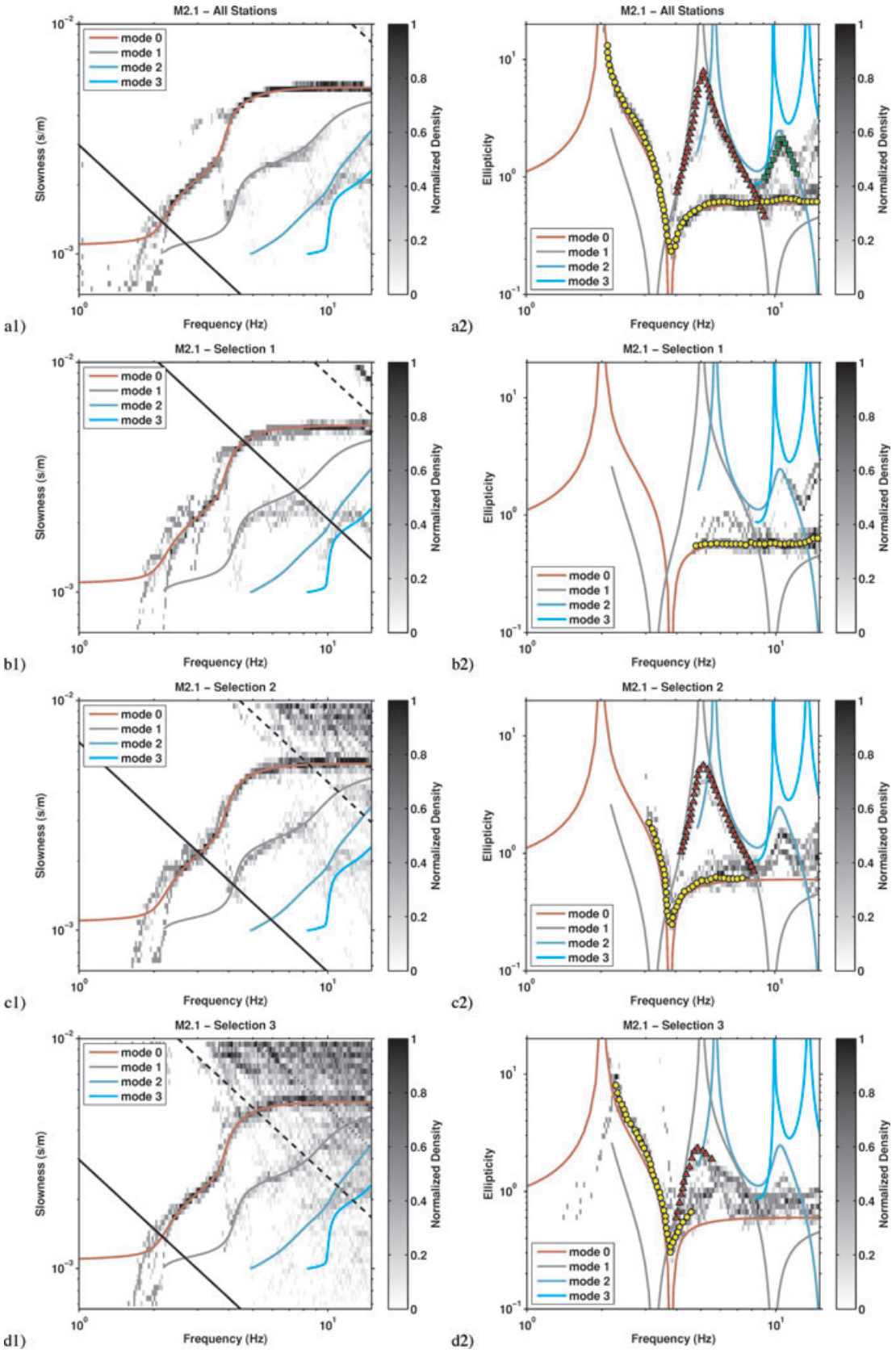

Figure 8. Dispersion and ellipticity probability distributions of the model M2.1. Statistics are performed using values picked from both vertical and horizontal-radial components. Resolution limits are included in the dispersion histograms ($k_{\min}$ with solid line, $k_{\max}/2$ with dashed line and $k_{\max}$ with dotted line). For clarity, the ellipticity values out of resolution range are not included. Manually picked ellipticity is thus presented (in yellow the fundamental mode, in red the first higher mode and in green the second higher) with theoretical curves for comparison (solid lines).

(Fig. 8c2). In this case the resolution limits match the high energy region of the first higher mode, clearly identifiable over a wide range of frequencies. Nothing can be obtained for the second mode, whose dispersion values cannot be picked. Finally, in 'selection 3', aliasing phenomena are unfortunately too close to the high energy region of the dispersion curves. This problem also reflects on ellipticity values for both the fundamental and first higher modes. Both progressively deviate from the true solution when they approach the Nyquist wavenumber limit (Fig. 8d2).

3.1.2 Model M10.2

The model M10.2 presents some additional structural complexity. Here, to simulate a moderate gradient of the shear wave velocity, two overlapping sedimentary layers are included. However, the longitudinal wave velocity contrast has been drastically reduced at the bedrock interface, a condition common for water-saturated sand or any analogous high-porosity material.

It is interesting to notice a phenomenon observable at about 5 Hz, where the fundamental mode Rayleigh wave gives rise to apparent bifurcation. This is our working hypothesis: the f–k method we use is based on the assumption of plane waves propagation, while in practice close noise sources generate spherical wave fronts. For this reason, on the horizontal component, a small fraction of Love waves will always be decomposed and projected onto the radial component. The array, therefore, will erroneously interpret this residual as a coherent (nevertheless very weak) in-plane wave propagation phenomena. The number of employed receivers and the array geometry influence the final result. It is not surprising that using all 39 available sensor locations, the Love wave contribution is clearly visible and undistorted (Fig. 9a1). Conversely, its influence is too weak to be correctly resolved if we use small configurations (Figs 9b1, c1 and d1). In such cases the result is mainly controlled by the range of resolution (e.g. comparing selections 1 and 3 at 4 Hz, respectively outside and inside the resolution limits) and other external factors like the local Rayleigh to Love energy ratio. The effect is less evident in model M2.1, even though it has the same receiver configuration and similar type and distribution of noise sources as model M10.2. Therefore, we assume that an increase in the Love waves energy contribution caused by the different velocity structures might be present.

Our results here are similar to those obtained from the elaboration of model M2.1 and are to a certain extent better. In particular, in 'selection 2', the second higher mode is now partially identifiable, even if in a narrow range of frequencies (Fig. 9c2). Moreover, in 'selection 3', the first higher mode is closer to the theoretical curve, although the fundamental mode is still slightly overestimated in the right flank of the curve (Fig. 9d2). That overestimation may occur because of the previously mentioned higher energy content of Love waves in this frequency range.

3.1.3 Model M11.2

This last synthetic model is the most complex, consisting of stacked horizontal soft layers with decreasing velocities (a negative gradient) down to the bedrock. Its dispersion pattern shows moderate complexity, with modal curves close to apparent intersection (Fig. 10a1). This sometimes leads to a difficulty in clearly identifying the correct slowness values in the histogram plot. Nevertheless, it is still possible to obtain good results for fundamental and higher modes.

The Rayleigh wave fundamental mode is always clearly identifiable when we use all four types of receiver configurations. The corresponding ellipticity is in most cases close to the theoretical solution (Fig. 10a2). An exception is present in the high frequency region above 12 Hz. Here the influence of the first higher mode is strong and reflects on the retrievable ellipticity, which in 'selection 1 and 2' is slightly underestimated (Figs 10b2 and c2). In 'selection 2', additionally, the fundamental mode ellipticity is definitely overestimated between 3 and 4 Hz.

Model M11.2, however, shows the smallest energy content of higher modes in comparison to the two previous tests. The first and second higher modes are reasonably identifiable if we use all available receivers, but ellipticity is only correctly retrieved for a limited portion of these modes. Furthermore, using the selected configurations 2 and 3, the frequency range where good results are obtainable is drastically reduced, because the dispersion curves of the higher modes are not clearly retrievable from the slowness–frequency plane (Figs 10c2 and d2). This problem is due to their low energy content. In such situations, we urge a conservative definition of ellipticity to avoid biased results.

3.2 Real test case: the town of Visp

To test the method in a real situation, we conducted an experiment at two different locations in the neighbourhood of the town of Visp in southern Switzerland. From a geological point of view, this area is a Quaternary sedimentary basin consisting of horizontally layered fluvial deposits (Roten *et al.* 2006, 2008). Despite the valley's typical V-shape, it is sufficiently wide to assume one-dimensionality, an assumption required by the frequency–wavenumber method and still valid for the upper layers. The total thickness of the basin progressively varies in relation to the distance from the valley axes. However, for our station locations, the depth of the bedrock can be locally estimated to be 100 m for 'Array 01' and 160 m for 'Array 02'. Also the topography at the measurement locations is not particularly irregular and a plane free surface can be assumed. The bedrock, constituted by gneiss in the northern part of the basin and metamorphosed mesozoic limestone in the south, ensures a moderate contrast of impedance at its interface.

For the first test location, a single array of 14 stations has been set up (Fig. 11). For the second, two separate array configurations with different radii were employed, of 14 ('configuration 1') and 11 ('configuration 2') stations, respectively. The acquisition was performed using 5 *s* triaxial velocimeters. For each array, together with dispersion curves and ellipticity results, the receiver geometry, the geographical location in the area of Visp and the results from single-station H/V spectral ratio analysis (Fig. 12) are thus presented.

3.2.1 Array 01

After frequency–wavenumber analysis of this data set, the Rayleigh dispersion curve for the fundamental mode is clearly retrievable in the frequency range between 3 and 12 Hz (Fig. 13a1). Although the histogram shows a moderate scattering of the picked values, the corresponding ellipticity is well identified. Most probably, higher modes are present in the wavefield, as indicated by the presence of high amplitude values in the ellipticity plot. However, the difficulty in following the corresponding dispersion curves in the slowness–frequency plane makes identifying the ellipticity extremely questionable. Nevertheless, we can separate these

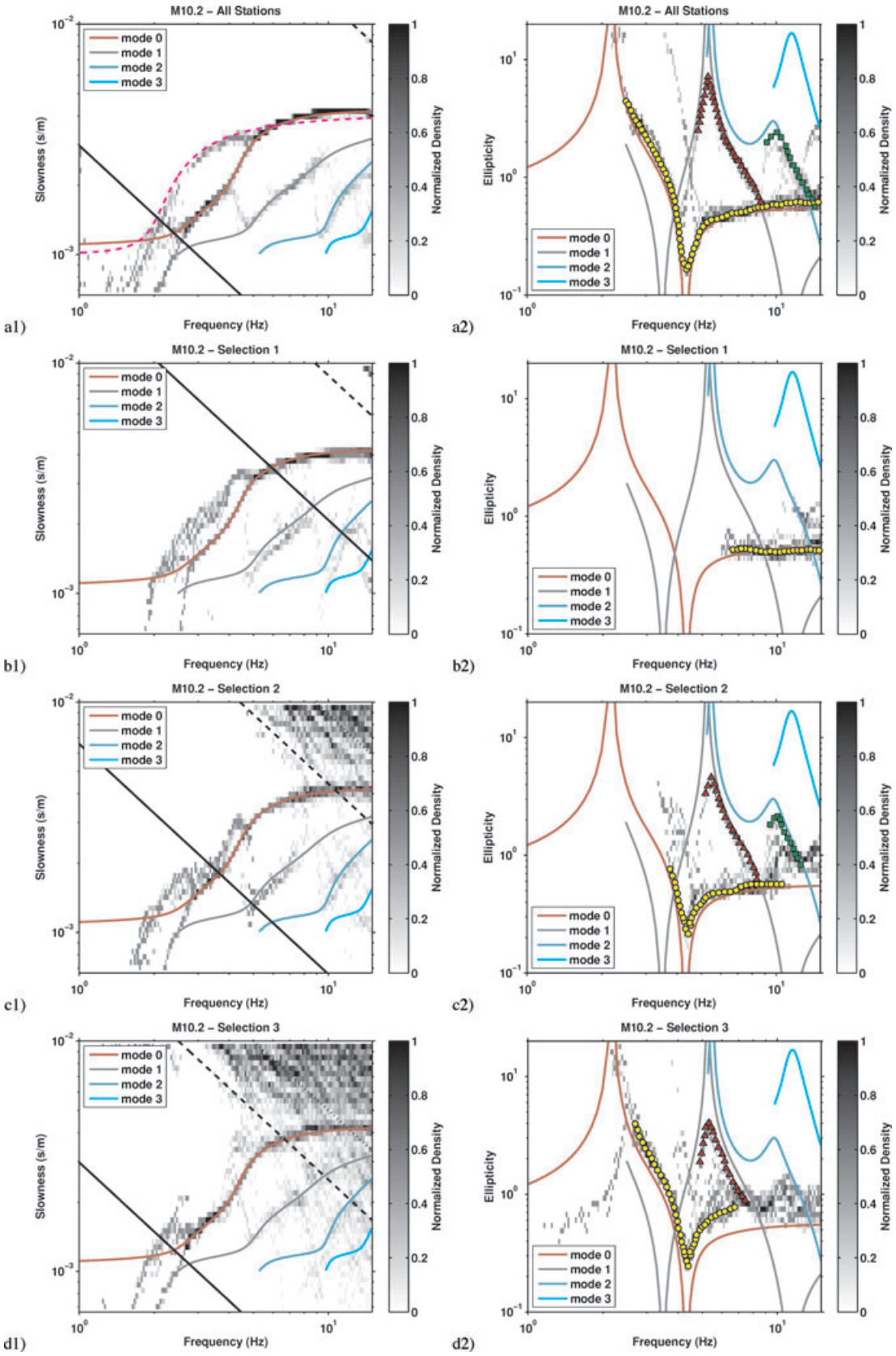

Figure 9. Dispersion and ellipticity probability distributions of the model M10.2. Results are comparable to those analyzed in data set M2.1. Here, however, the influence of Love waves fundamental mode might be stronger (a1, dashed magenta line) and not entirely removable by polarization analysis, as can be inferred from the apparent bifurcation of the observed Rayleigh dispersion curve.

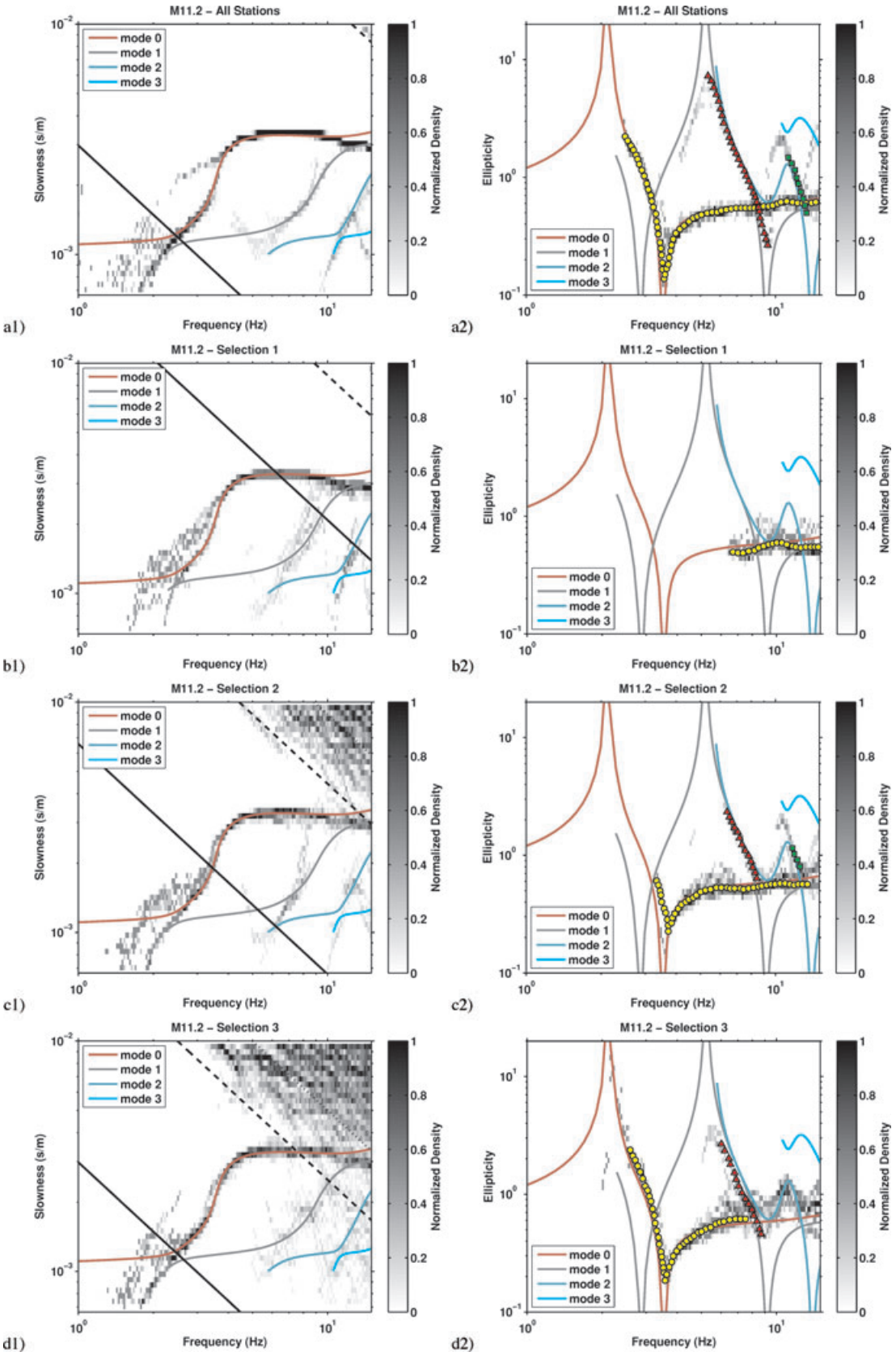

Figure 10. Dispersion and ellipticity probability distributions of the model M11.2. This case represents one of the most complex, because the shear wave velocity has a negative gradient. Identifying the correct dispersion curve is not always possible, especially for higher modes, due to apparent intersection of modes at specific frequencies.

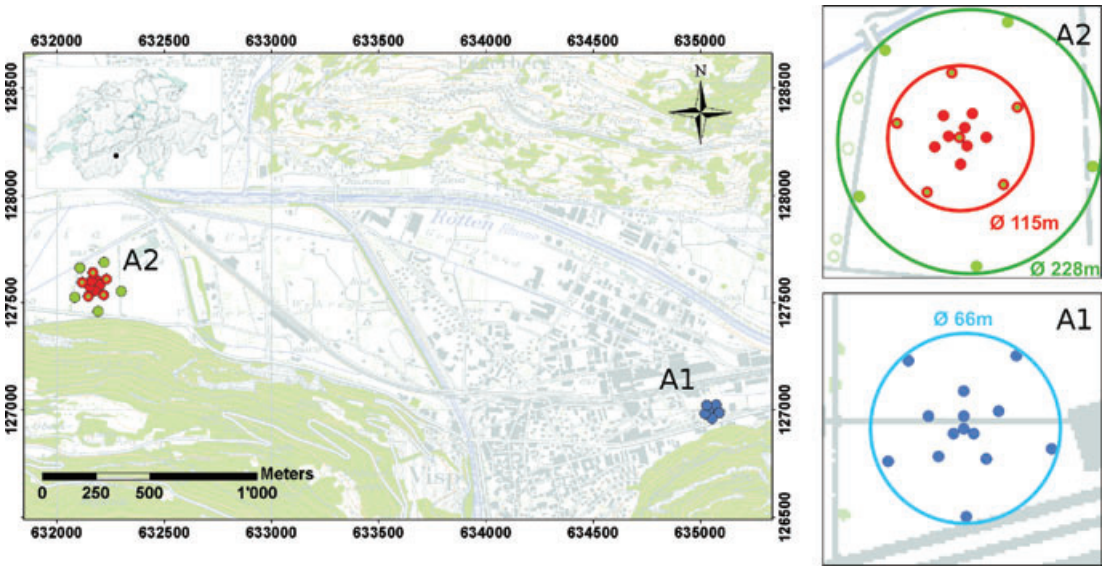

Figure 11. Location of the two array measurement sites in the area of Visp (Switzerland). Units are in Swiss coordinates. For the 'array 01' test, a single configuration of 14 receivers was used (in blue). For the 'array 02' test, two overlapping configurations of 14 (in red) and 11 receivers (in green) were employed separately.

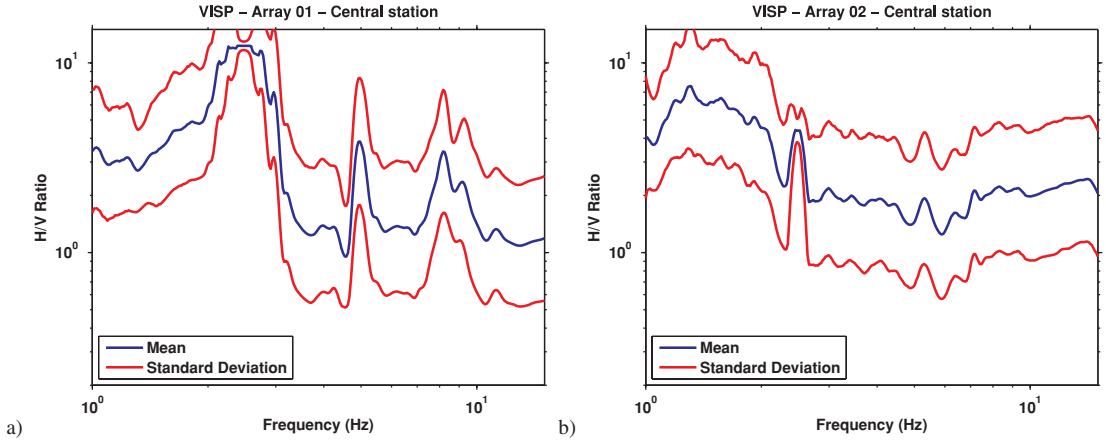

Figure 12. Standard single-station H/V spectral ratios from the central sensor of 'array 01' and 'array 02' in Visp. The two curves are visibly affected by a disturbance around 2.5 Hz, presumably of industrial origin (a pump or a compressor), which is also observed on the entire Rhone plain.

contributions from the fundamental mode, a feature not possible using single-station H/V spectral ratios (Fäh *et al.* 2008).

3.2.2 Array 02

To extend the frequency range of resolution, the 'Array 02' experiment was performed with two separate configurations of increasing diameter. From the analysis of 'configuration 1', we obtained good results. The fundamental mode dispersion curve is clearly identifiable, and the corresponding ellipticity is also well defined (Figs 13b1 and b2). In contrast, identifying higher mode dispersion is more complex but possible if we compute and compare several different elaborations. We must adjust progressively the processing parameters such as the tolerance level for relative maxima identification in the slowness–azimuth plane, and the number of aggregation classes of the histogram distribution. The ellipiticities of the first and second higher modes appear reliable, showing a pattern similar to those obtained from synthetic models.

'Configuration 2' extended the resolution limits of the previous elaboration to lower frequencies (Figs 13c1 and c2). The fundamental mode matches reasonably well the results obtained from 'configuration 1' for dispersion and ellipticity. For higher modes, the same scheme of elaboration previously introduced has been employed. However, slight differences are observable. In particular, the amplitude of the first higher mode is shifted to lower values, when compared with the corresponding curves obtained from 'configuration 1'. In practice this can be induced, other than by the influence of aliasing, because in real cases approximating a perfect 1-D structure is not strictly valid. Indeed, an array of such large aperture may sample the wavefield at points where the ground conditions are not perfectly identical. This would influence the higher modes that

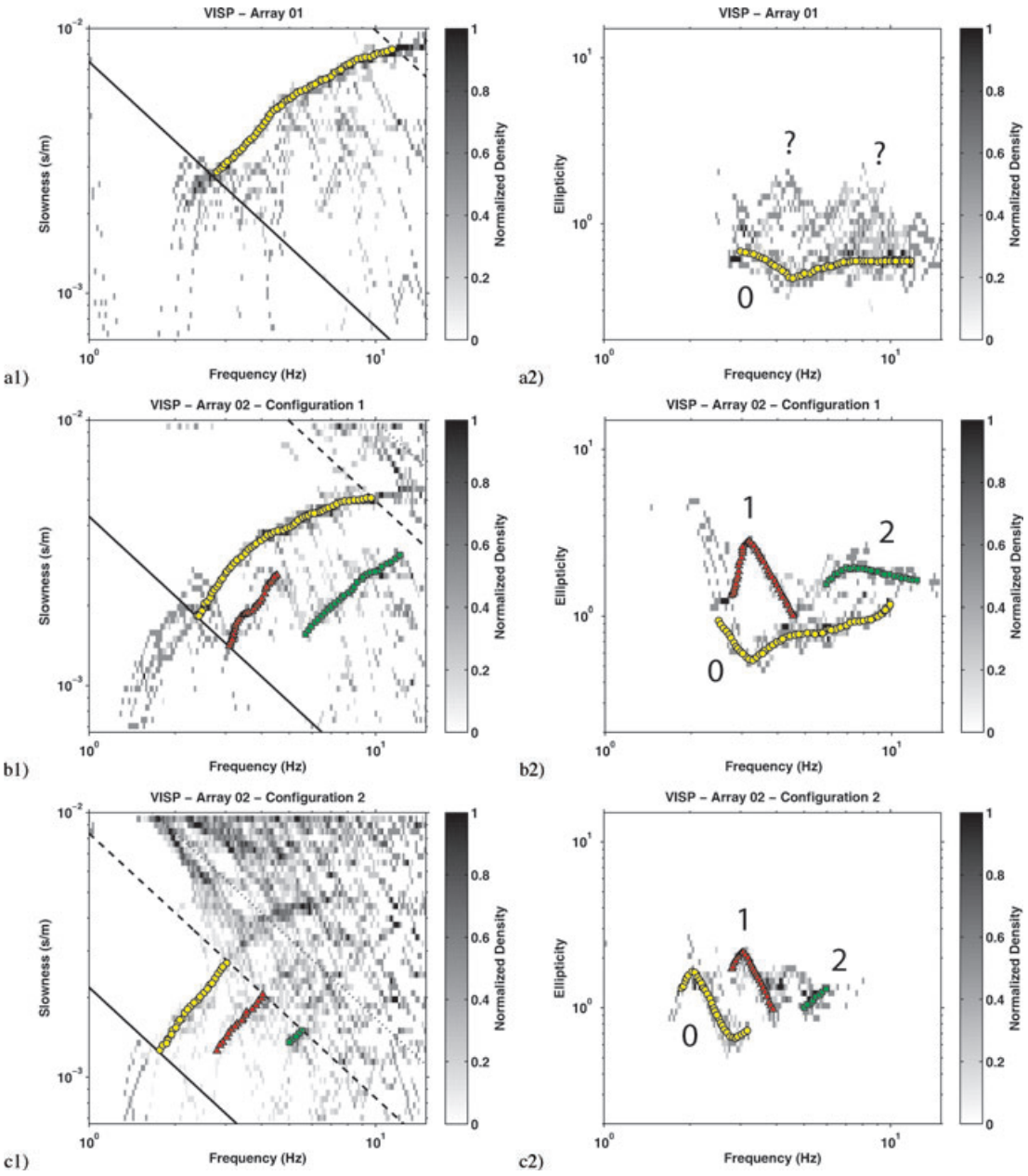

Figure 13. Dispersion and ellipticity probability distributions of the two array measurements performed in Visp. As in the previous cases, the curves are manually extracted for dispersion and ellipticity (in yellow the fundamental mode, in red the first higher mode and in green the second). To make results qualitatively comparable, all graphs are presented with the same scale used for synthetics. As expected from the corresponding receiver geometry, curves from 'configuration 1 and 2' partially overlap.

are generally more sensitive than the fundamental to small-scale variability.

4 DISCUSSION AND CONCLUSIONS

The frequency–wavenumber method we propose can retrieve the ellipticity of Rayleigh waves for the fundamental and, with some limitations, higher modes. In comparison to single-station H/V spectral ratios, we can now distinguish and separate the different wave types and, consequently, minimize the influence of Love waves. The amplitude distortion due to *SH* standing waves is automatically removed within beamforming by destructive interference of the out-of-phase contributions.

Reliable results are obtainable for the fundamental mode of Rayleigh waves, but reasonable results are also achievable for higher modes, whenever the corresponding dispersion curve is well identified in the slowness–frequency plane. We notice some slight difference between the values of ellipticity obtained from separately identifying maxima on the vertical and the horizontal components. Amplitude ratios from signals picked on vertical components are generally more stable over the whole frequency range and closer to theoretical ellipticity. By contrast, results obtained from analysing the horizontal-radial direction tend to be slightly overestimated

(∼5–10 per cent, depending on the number of receivers), especially at high frequencies. This result is probably due to the residual influence of *SH* waves on that component. In this second case, however, identifying higher mode dispersion is generally more accurate. We suggest the combined and simultaneous use of the two components to compensate for the contributions and improve the final statistics.

The quality of retrievable ellipticity curves depends on the complexity of the structural model, the array geometry and the noise level. We notice that dispersion curves close to apparent intersection (phase velocity differs less than about 50 m s^{-1}) can produce deviations of the amplitude values, due to the difficulty that the adaptive filter has in separating the different contributions. Signals with a low energy content that can hardly be resolved in the slowness–frequency plane can lead to unreliable ellipticity values. As a general rule, signals with a power amplitude lower than about two times the average noise power level should be rejected. A progressive reduction in the number of the employed seismic receivers drastically restricts the resolution of the method. This will occur for resolution bounds and amplitude distortion. Sparse spatial sampling can lead to insufficient minimization of the body waves, as well as progressively increased distortion induced by uncorrelated noise. We suggest the use of a number of receivers higher than 15, but in any case not less than 10, to reconstruct the correct ellipticiy. Moreover, if the receiver configuration is too irregular, the presence of high-amplitude sidelobes in the beampattern cannot be completely minimized by the adaptive filtering. That effect introduces a progressive scattering in the results. Thus, we suggest optimization of the array geometry.

When different array configurations of increasing size and overlapping resolution bounds are available, we must compare the corresponding segments of ellipticity and dispersion curves to place additional quality control on the final results. Portions of curves that present a good agreement between different configurations can be considered a reasonable measure of true ellipticity. In contrast, we suggest a conservative approach in cases of progressive mismatch: avoid those curves that lack a clear behaviour or those whose corresponding mode of propagation cannot be unequivocally defined. This is particularly important with real complex structures, where the local variability might lead to large deviations in surface wave velocity and energy content (especially for higher modes) within small distances.

The possibility of including the retrieved ellipticity as a constraint for inverting structural models is, at the moment, in the testing phase and no definitive conclusions are yet possible. A more accurate analysis in this direction is planned, and the improvement in using this technique for site characterization will be examined. However, further investigations must be performed on the proposed method to explore its full possibility and application.

ACKNOWLEDGMENTS

This research was supported by the Swiss National Science Foundation within the project HAZARD 2010 (No. 200021-112284) and also by the projects NERIES (Network of Research Infrastructures for European Seismology, task JRA4 - 'Geotechnical site characterization') and COGEAR (Coupled seismogenic Geohazards in Alpine Regions). A special thank you to Marc Wathelet for providing the software package 'Geopsy' (http://www.geopsy.org) that enabled us to test our results. I appreciate all his hints during this last year of work. I also acknowledge our GJI anonymous reviewers, for their helpful comments and suggestions, and our English editors, Dr Kathleen Jackson and Dr Benjamin Edwards. A final thanks goes to Dr Jan Burjanek and Stefano Maranò for reviewing the linear algebra of the paper.

REFERENCES

Arai, H. & Tokimatsu, K., 2004. S-wave velocity profiling by inversion of microtremor H/V spectrum, *Bull. seism. Soc. Am.,* **941,** 53–63.

Asten, M.-W., 1976. The use of microseisms in geophysical exploration, *PhD thesis*, Macquarie University, Australia.

Asten, M.-W., 2006. On bias and noise in passive seismic data from finite circular array data processed using SPAC methods, *Geophysics,* **71**(6), 153–162.

Asten, M.-W. & Henstridge, J.-D., 1984. Array estimators and the use of microseisms for reconnaissance of sedimentary basins, *Geophysics,* **49,** 1828–1837.

Asten, M.-W., Dhu, T. & Lam, N., 2004. Optimised array design for microtremor array studies applied to site classification; observations, results and future use, in *Proceedings of the 13th World Conference of Earthquake Engineering*, Vancouver, Paper 2903.

Bonnefoy-Claudet, S., Cotton, F. & Bard, P.-Y., 2006a. The nature of noise wavefield and its applications for site effects studies: a literature review, *Earth-Sci. Rev.,* **79,** 205–227.

Bonnefoy-Claudet, S., Cornou, C., Bard, P.-Y., Cotton, F., Moczo, P., Kristek, J. & Fäh, D., 2006b. H/V ratio: a tool for site effects evaluation. Results from 1D noise simulation, *Geophys. J. Int.,* **167,** 827–837.

Capon, J., 1969. High resolution frequency wavenumber spectrum analysis, *Proc. IEEE,* **57,** 1408–1418.

Fäh, D., Kind, F. & D. Giardini, 2001. A theoretical investigation of average H/V ratios, *Geophys. J. Int.,* **145,** 535–549.

Fäh, D., Kind, F. & Giardini, D., 2003. Inversion of local S-wave velocity structures from average H/V ratios and their use for the estimation of site-effects, *J. Seismol.,* **7,** 449–467.

Fäh, D., Stamm, G. & Havenith, H.-B., 2008. Analysis of three-component ambient vibration array measurements, *Geophys. J. Int.,* **172,** 199–213.

Haubrich, R.-I., 1968. Array design, *Bull. seism. Soc. Am.*, 58-3, 977–991.

Hisada, Y., 1994. An efficient method for computing Green's functions for a layered half-space with sources and receivers at close depth, *Bull. seism. Soc. Am.,* **84,** 1456–1472.

Horike, M., 1985. Inversion of phase velocity of long-period microtremors to the S-wave-velocity structure down to the basement in urbanized areas, *J. Phys. Earth,* **33,** 59–96.

Kind, F., Fäh, D. & Giardini, D., 2005. Array measurements of S-wave velocities from ambient vibrations, *Geophys. J. Int.,* **160,** 114–126.

Kogon, S.-M., 2003. Eigenvectors, diagonal loading and white noise gain constraints for robust adaptive beamforming, *Signals, Syst. Comput.,* **2,** 1853–1857.

Köhler, A., Ohrnberger, M., Scherbaum, F., Wathelet, M. & Cornou, C., 2007. Assessing the reliability of the modified three-component spatial autocorrelation technique, *Geophys. J. Int.,* **168**(2), 779–796.

Lachet, C. & Bard, P.-Y., 1994. Numerical and theoretical investigations on the possibilities and limitations of Nakamuras technique, *J. Phys. Earth,* **42,** 377–397.

Lacoss, R.-T., Kelly, E.-J. & Toksz, M.-N., 1969. Estimation of seismic noise structure using arrays, *Geophysics,* **34,** 21–38.

Li, T.-M.-C., J.-F. Ferguson, E. Herrin & H.-B. Durham, 1984. High-frequency seismic noise at Lajitas, Texas, *Bull. seism. Soc. Am.,* **74,** 2015–2033.

Marzetta, T., 1983. A new interpretation for Capon's maximum likelihood method of frequency–wavenumber spectral estimation, *Proc. ICASSP 84,* **31,** 445–449.

Nakamura, Y., 1989. A method for dynamic characteristics estimation of subsurface using microtremor on the ground surface, Rep. Railway Tech. Res. Inst., Jpn 30 1, 2533.

Nogoshi, M. & Igarashi, T., 1971. On the amplitude chatacteristics of microtremors. Part 2 (in Japanese with English abstract), *J. Seism. Soc. Japan,* **24,** 26–40.

Okada, H., 2003. The microseismic survey method: Society of Exploration Geophysicists of Japan. Translated by Koya Suto, Geophysical Monograph Series, No. 12, Society of Exploration Geophysicists, Tulsa.

Park, C.-B., Miller, R.-D. & Xia, J., 1999. Multichannel analysis of surface waves, *Geophysics,* **64,** 800–808.

Parolai, S., Picozzi, M., Richwalski, S.-M. & Milkereit, C., 2005. Joint inversion of phase velocity dispersion and H/V ratio curves from seismic noise recordings using a genetic algorithm, considering higher modes, *Geophys. Res. Lett.,* **32,** 1, L01303.

Roten, D., Fäh, D., Cornou, C. & Giardini, D., 2006. Two-dimensional resonances in Alpine valleys identified from ambient vibration wavefields, *Geophys. J. Int.,* **165,** 889–905.

Roten, D., Fäh, D., Olsen, K.-B. & Giardini, D., 2008. A comparison of observed and simulated site response in the Rhne valley, *Geophys. J. Int.,* **173,** 958–978.

Sibul, L.-H., 1984. Application of singular value. decomposition to adaptive beamforming, *Proc. ICASSP 84,* **9,** 750–753.

Strobbia, C., 2003. Surface wave method: acquisition, processing and inversion, *PhD thesis*, Politecnico di Torino.

Tokimatsu, K., 1997. Geotechnical site characterization using surface waves, in *Proceedings of the 1st International Conference of Earthquake Geotechnical Engineering*, Ishihara (ed), Balkema, 1333–1368.

Wathelet, M., 2005. Array recordings of ambient vibrations: surface-wave inversion, *PhD thesis*, University of Lige, Belgium.

Wathelet, M., Jongmans, D., Ohrnberger, M. & Bonnefoy-Claudet S., 2008. Array performances for ambient vibrations on a shallow structure and consequences over Vs inversion, *J. Seismol.,* **12**(1), 1–19.

Woods, J.-W., Lintz, P.-L, 1973. Plane waves at small arrays, *Geophysics,* **38,** 1023–1041.

Yamanaka, H., Takemura, M., Ishida, H. & Niwa, M., 1994. Characteristics of long-period microtremors and their applicability in exploration of deep sedimentary layers, *Bull. seism. Soc. Am.,* **846,** 1831–1841.

Zywicki D.-J., 1999. Advanced signal processing methods applied to engineering analysis of seismic surface waves, *PhD thesis*, Georgia Institute of Technology, Atlanta, USA.

SUPPORTING INFORMATION

Additional Supporting Information may be found in the online version of this article:

Movie. 3-D plot showing the relation between Rayleigh particle motion (ellipticity), slowness and frequency. Processing has been done with three-component array analysis. Colours are as for Fig. 5.

Please note: Wiley-Blackwell are not responsible for the content or functionality of any supporting materials supplied by the authors. Any queries (other than missing material) should be directed to the corresponding author for the article.